Journal of Biomedical Optics

SPIEDigitalLibrary.org/jbo

Dual-wavelength photothermal optical coherence tomography for imaging microvasculature blood oxygen saturation

Biwei Yin
Roman V. Kuranov
Austin B. McElroy
Shams Kazmi
Andrew K. Dunn
Timothy Q. Duong
Thomas E. Milner

Dual-wavelength photothermal optical coherence tomography for imaging microvasculature blood oxygen saturation

Biwei Yin,[a] Roman V. Kuranov,[b] Austin B. McElroy,[c] Shams Kazmi,[c] Andrew K. Dunn,[c] Timothy Q. Duong,[b] and Thomas E. Milner[c]
[a]University of Texas at Austin, Departments of Electrical and Computer Engineering, 1 University Station C0803, Austin, Texas 78712
[b]University of Texas Health Science Center at San Antonio, Department of Ophthalmology, 7703 Floyd Curl Drive, San Antonio, Texas 78229
[c]University of Texas at Austin, Department of Biomedical Engineering, 1 University Station C0800, Austin, Texas 78712

Abstract. A swept-source dual-wavelength photothermal (DWP) optical coherence tomography (OCT) system is demonstrated for quantitative imaging of microvasculature oxygen saturation. DWP-OCT is capable of recording three-dimensional images of tissue and depth-resolved phase variation in response to photothermal excitation. A 1,064-nm OCT probe and 770-nm and 800-nm photothermal excitation beams are combined in a single-mode optical fiber to measure microvasculature hemoglobin oxygen saturation (SO_2) levels in phantom blood vessels with a range of blood flow speeds (0 to 17 mm/s). A 50-μm-diameter blood vessel phantom is imaged, and SO_2 levels are measured using DWP-OCT and compared with values provided by a commercial oximeter at various blood oxygen concentrations. The influences of blood flow speed and mechanisms of SNR phase degradation on the accuracy of SO_2 measurement are identified and investigated. [DOI: 10.1117/1.JBO.18.5.056005]

Keywords: optical coherence tomography; dual-wavelength; imaging; phase-sensitive; microvasculature; hemoglobin oxygen saturation; phantom.

Paper 130033R received Jan. 21, 2013; revised manuscript received Mar. 5, 2013; accepted for publication Mar. 26, 2013; published online May 2, 2013.

1 Introduction

Noninvasive quantitative evaluation of microvasculature hemoglobin oxygen saturation (SO_2) in tissue is important in early detection and monitoring the progression of inflammatory and ischemic diseases such as cancer, stroke, and glaucoma.[1,2] Various approaches have been used to assess *in vivo* microvascular oxygen saturation, including oxygen-sensitive microelectrodes,[3–7] magnetic resonance imaging (MRI),[8–12] reflection spectroscopic oximetry.[13–18] and phosphorescence quenching.[17,19–24] Measurement by oxygen-sensitive microelectrodes is a point measurement method and is primarily limited to animal studies. MRI has limited spatial (100 to 150 μm) and temporal (tens of seconds to minutes) resolution. The phosphorescence quenching technique has limited spatial resolution (e.g., 50 μm), and no oxygen sensitive dyes that are approved by the United States Food and Drug Administration are available for clinical translation.

A useful three-dimensional imaging technique, optical coherence tomography (OCT), was introduced in 1991 as a time domain approach[25] and was later used as a frequency domain method.[26,27] OCT implementation in the frequency domain improves signal-to-noise ratio and allows high-speed image acquisition. More recently, Huber et al. showed that, for an equivalent signal-to-noise ratio, swept-source (SS) OCT with balanced detection provides higher acquisition rates compared with spectrometer-based Fourier domain OCT approaches.[28]

Biomedical investigators are interested in applying OCT approaches to measure microvasculature SO_2 in tissues. Spectroscopic Fourier domain OCT (SFD-OCT)[29,30] has been reported to measure depth-resolved microvasculature oxygenation, but an appropriate model has not been given to estimate the attenuation coefficients required to determine blood SO_2 levels using OCT light in the near infrared spectral region.[31] SFD-OCT has been shown to provide sufficient sensitivity to quantify micro vascular SO_2 levels using visible wavelengths (460 to 700 nm) where hemoglobin absorption is relatively large.[32,33] However, SFD-OCT using visible wavelength sources is compromised by limited imaging depth, which is restricted by increased scattering.

Photothermal OCT is a functional imaging technique that can measure the optical pathlength variation of OCT light backscattered from tissues in response to an excitation beam. Adler has demonstrated photothermal OCT using a gold nanoparticle contrast agent.[34] Skala has developed photothermal OCT for high-resolution molecular imaging,[35] and Paranjape has reported using photothermal OCT to detect macrophages in tissue.[36] So far, reported applications of photothermal OCT have focused primarily on light absorption by nanoparticles. Previously, we reported using dual-wavelength photothermal OCT (DWP-OCT) to measure microvasculature SO_2 in both phantom[37] and *in vivo*[38] blood vessels using a common-path phase-sensitive (PhS) OCT system.[39] Because we used a common path interferometer, imaging by scanning the beam was difficult, and the results were limited to point microvasculature SO_2

Address all correspondence to: Roman V. Kuranov, University of Texas Health Science Center at San Antonio, Department of Ophthalmology, 7703 Floyd Curl Drive, San Antonio, Texas 78229. Tel: 210-567-8402; Fax: 210-567-8413; E-mail: rkuranov@yahoo.com

measurement. In this study, we report a DWP-OCT system that uses a two-beam interferometer and allows for the imaging and measurement of SO_2 levels.

Compared to two-beam interferometers, common path interferometry provides higher sensitivity and stability to measure the phase of interference fringes of light backscattered from transparent and scattering media. Despite these advantages, several drawbacks of prior common-path DWP-OCT system[37–39] design are recognized. Recording en-face images is challenged by incorporating a 2D scanning system into the sample arm. A short working distance associated with common-path DWP-OCT introduces problems for positioning the OCT probe beam at a desired sample measurement location. Also, the short working distance makes intravascular, retinal, and endoscopic applications challenging. We present a DWP-OCT system using a fiber two-beam interferometer to image and measure SO_2 levels in a phantom blood vessel.

2 Methods

2.1 *DWP-OCT System*

In this study, a DWP-OCT system using a fiber Michelson interferometer was constructed for imaging and blood SO_2 measurement. Interferometric fringe phase stabilization is a critical feature required for SO_2 measurement. In a generic phase-sensitive SS OCT system, two mechanisms contribute to phase noise: inconsistency of the start wavelength between successive A-scans, and nonspecific mechanical movement of optical elements in sample and reference arms. To resolve the first issue, 5% of light in the sample arm is coupled to a high-reflectivity mirror, which is sufficient to form a high SNR interference fringe signal with reference light but too weak to introduce an artifactual autocorrelation and interference signal with light backscattering from the sample. Light reflecting from a high-reflectivity mirror in the sample path introduces a feature-line in recorded B-scans positioned below the imaging media and does not compromise image quality. To minimize the second source of phase noise (due to nonspecific mechanical movement of optical elements), the sample beam scanning system is constructed using a stable mechanical cage system.

Blood SO_2 measurement value is dependent on the ratio (χ) of optical pathlength (op) signal amplitude at modulation frequencies introduced by 770-nm and 800-nm photothermal excitation light. To balance incident fluence of photothermal excitation beams, the scanning optics is designed to provide nearly equivalent spot sizes for 770-nm and 800-nm light.

The DWP-OCT system (Fig. 1) for imaging and blood SO_2 measurement consists of two major systems: a SS PhS OCT system that provides accurate depth-resolved phase measurement with a 300-pm lower bound of detectable op signal amplitude, and two excitation lasers (770 and 800 nm) that are intensity modulated at 400 and 380 Hz, respectively, and introduce a nanometer-scale harmonic op signal amplitude due to blood absorption.

The phase-sensitive OCT system uses a swept source laser (HSL-1000, Santec Corp. Komaki, Aichi, Japan) with a 28-kHz A-line rate, a center wavelength at 1,060 nm, and full-wave-half-maximum spectral width of 58 nm. Single-mode optical fiber (HI1060, Corning Inc., Corning, NY) is utilized to construct the interferometer. Light emitted by the SS laser is split into three subsystems: trigger, sampling clock, and signal interferometer.

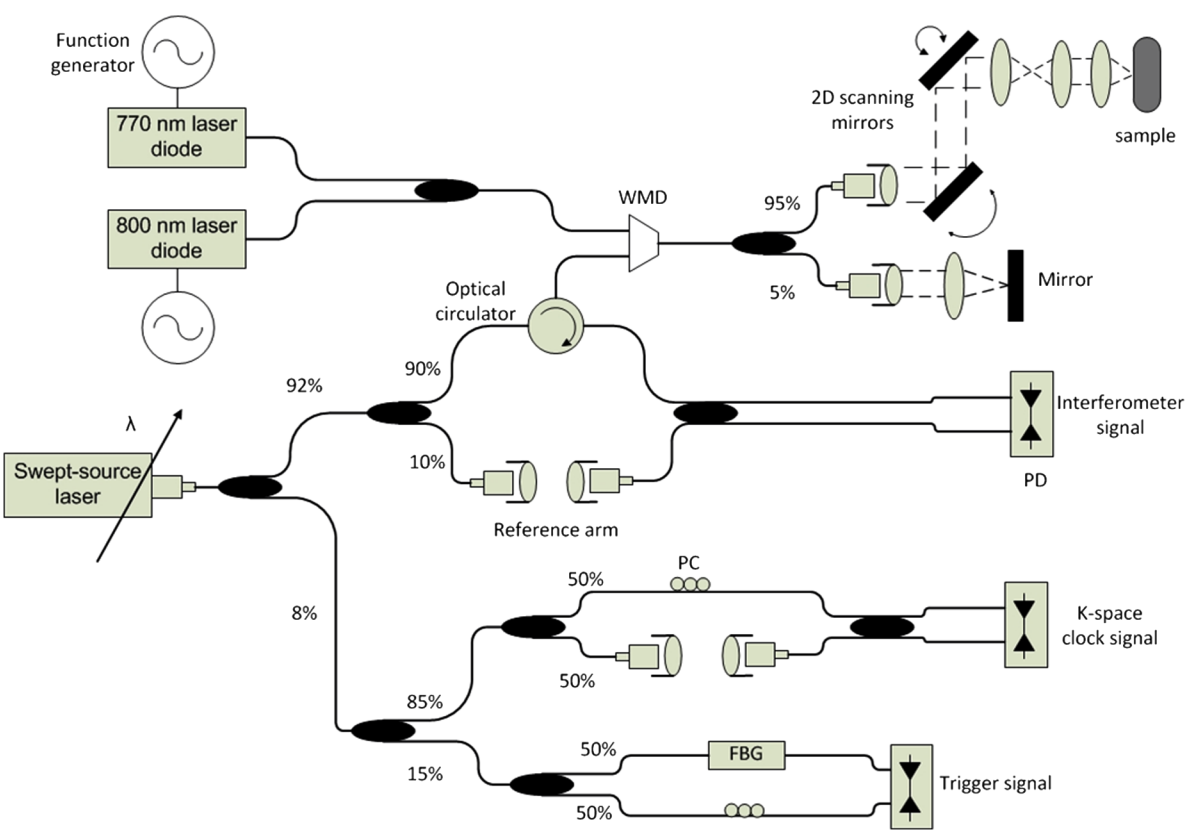

Fig. 1 DWP-OCT system schematic. WDM: wavelength division multiplexer, FBG: fiber Bragg grating, PC: polarization controller, PD: photodetector.

The trigger subsystem utilizes a fiber Bragg grating (FBG) to ensure the digitizer starts data acquisition at a consistent and repeatable wavenumber for each A-scan. The sampling clock subsystem consists of a Mach-Zehnder interferometer with a clock rate set by adjusting the interferometric light delay. The sampling clock signal received by a balanced photodetector is input into an external analog circuit, frequency quadrupled, and used as a sampling trigger for the analog-to-digital converter.[40] The third subsystem is the Michelson signal interferometer with sample and reference arms. An optical circulator (1060 PI TGG, Agiltron Inc., Woburn, MA) is used in the sample arm of the Michelson interferometer to increase SNR.[41] The sample arm contains two light paths: a path to the phantom blood vessel with an achromatic scanning system (consisting of two galvanometers and an afocal telescope), and a high-reflectivity mirror used for phase stabilization. The achromatic scanning system is designed and simulated in optical design software (Zemax, Radiant Zemax LLC, Redmond, WA) and provides micrometer-scale lateral resolution for imaging three co-aligned beams; the computed diffraction encircled energy computation gives a 13-μm lateral resolution for 770-nm and 800-nm excitation beams, along with a 14-μm resolution for the 1,060-nm PhS-OCT probe beam.

After the interference fringe signal is acquired uniformly in wavenumber (or optical frequency), computing a fast Fourier transform (FFT) of the signal, we obtain a complex number data array for each A-scan. The complex number amplitude is used to construct an OCT intensity image, and the complex number angle is used to determine the phase of the depth-resolved fringe signal. The signal phase of light reflecting from the mirror in the sample path is utilized to correct for any error introduced by delay in data acquisition. Phase errors at any sample depth (d_s) are eliminated by subtracting the reference phase scaled by depth from the sample phase[42] as

$$\varphi_{sc} = \varphi_s - \frac{d_s}{d_r}\varphi_r, \tag{1}$$

where φ_{sc} is the corrected sample phase, φ_s is the sample phase acquired from the raw signal FFT, φ_r is the reference phase obtained from interference between light reflected from the mirror in the sample path and the reference arm, and d_s and d_r are the sample and reference depths, respectively.

The system operates in real-time in either OCT intensity imaging or M-mode phase imaging. Data acquisition and signal processing software are written in Labview (National Instrument Corp., Austin, TX). The system sensitivity is 102 dB (with shot-noise limited sensitivity of 107 dB), and the axial resolution is 13 μm in tissue with the application of a real-time digital dispersion compensationalgorithm.[43,44] The axial resolution is limited by polarization mode dispersion in the circulator. After Fourier transform of M-mode phase data (i.e., 1-s duration), with a calibration process, the phase of light backscattered from a selected sample depth is converted to the optical pathlength ($op = \lambda * \phi_{sc}/2\pi$, where λ is the center wavelength and ϕ_{sc} is the corrected sample phase). The mean noise level in the signal frequency region corresponding to the intensity modulation of photothermal excitation light (360 to 420 Hz) is taken as the op signal noise floor and measured at 300 pm.

Photothermal excitation beams are emitted from two 100-mW single-mode fiber (HI780, Corning Inc., Corning, NY) pigtailed laser diodes (QFLD-780-100S,QPhotonics LLC, Ann Arbor, MI for 770 nm and QFLD-795-100S for 800 nm). Light from these sources is coupled into the DWP-OCT system's sample arm through a wavelength division multiplexer (WDM) (PSK-000851, Gould Fiber Optics, Millersville, MD). Both the WDM and the PhS-OCT system are constructed using HI1060 Corning fiber, which is single-mode fiber for 1,060-nm probe light and allows two or three propagation modes at photothermal excitation wavelengths of 770 nm and 800 nm. The temperature of each laser diode is precisely controlled within a fraction of a degree (K) and selected to ensure emission at the desired wavelength as calibrated using a spectrometer. The photothermal excitation power incidents on the sample for 800-nm and 770-nm wavelengths are 2.78 mW and 2.87 mW, respectively; both are within ANSI limits for skin. Intensity modulation frequencies for photothermal excitation light [770 nm (400 Hz) and 800 nm (380 Hz)] are selected in a signal frequency range where the phase noise is low (0.3 nm) and the op signal amplitude is high. The procedure for determining the optimum photothermal excitation frequency to maximize op signal-to-noise ratio for blood was reported previously.[38] OCT probe (1,064-nm) and photothermal excitation (770-nm and 800-nm) beams are co-aligned and coincident on the sample.

2.2 SO_2 Calculation

We assume that op signal amplitude due to absorption by blood is linear with the fluence of photothermal excitation light,[45] as derived and reported previously.[37,38] Neglecting the effect of thermal diffusion, SO_2 level can be estimated from op measurement in response to 770-nm (1) and 800-nm (2) photothermal excitation.

$$SO_2 = \frac{c_0}{c_0 + c_d} = \frac{\alpha_{d1} - \chi_{12}\alpha_{d2}}{\chi_{12}(\alpha_{o2} - \alpha_{d2}) - (\alpha_{o1} - \alpha_{d1})}, \tag{2}$$

where c_o is the concentration of oxygenated hemoglobin (mM); c_d is the concentration of deoxygenated hemoglobin (mM); $\chi_{12} = (op_1/\Phi_1)/(op_2/\Phi_2)$; op is the measured optical pathlength signal amplitude; $\Phi = \tau I$ represents the fluence over one period;τ is the period of photothermal excitation; I is the average intensity of excitation light on the blood vessel; α_o and α_d are the tabulated molar extinction coefficients of oxygenated and deoxygenated hemoglobin ($cm^{-1}\,mM^{-1}$), respectively; and subscripts 1 (770 nm) and 2 (800 nm) correspond to the wavelengths of excitation light ($\alpha_{o1} = 0.65\ cm^{-1}\,mM^{-1}$, $\alpha_{o2} = 0.79\ cm^{-1}\,mM^{-1}$, $\alpha_{d1} = 1.312\ cm^{-1}\,mM^{-1}$, $\alpha_{d2} = 0.793\ cm^{-1}\,mM^{-1}$). The ratio of the two excitation beams' fluence (Φ_2/Φ_1) at the sample is calibrated before measurement. The op signal amplitude at each photothermal excitation wavelength (op_1 and op_2) is determined by computing the magnitude of the signal phase oscillation at the respective modulation frequencies of excitation light (Fig. 2).

2.3 Blood Vessel Phantom and Blood Flow

A 50-μm inner diameter polytetrafluoroethylene conduit (SUBL 060, Braintree Scientific Inc., Braintree, MA) containing porcine blood is used as a blood vessel phantom. A desired blood SO_2 level is achieved by adding sodium dithionite to the blood sample to deoxygenate. Six blood samples are prepared at different SO_2 levels (99.6%, 89.2%, 84.1%, 69.0%, 57.3%, and 3.0%). To provide a scattering background for imaging, the phantom blood vessel is placed on a sheet of

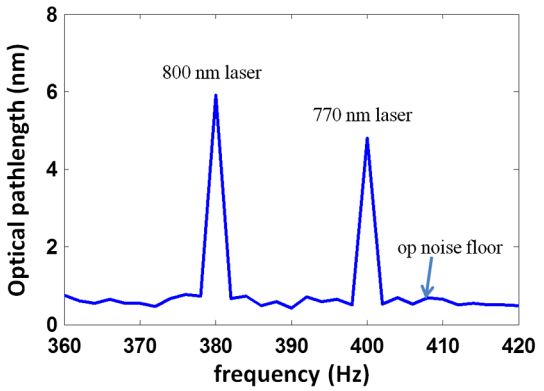

Fig. 2 Spectra of *op* signal amplitude induced by 770-nm (5-nm, 400-Hz) and 800-nm (6-nm, 380-Hz) excitation light.

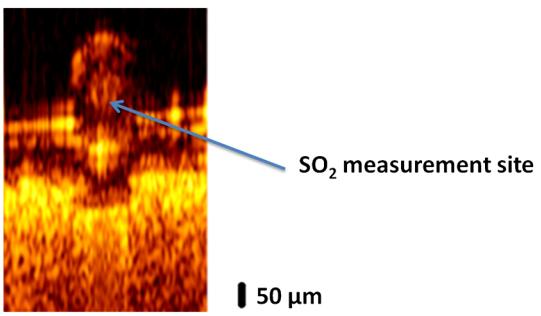

Fig. 3 B-scan image of a phantom vessel with a 50-μm inner diameter containing blood positioned on a sheet of white-colored copy paper.

white-colored copy paper. After imaging, blood SO_2 measurements are recorded in an M-mode acquisition at a selected position in the lumen of the phantom vessel (Fig. 3).

To investigate the effect of blood flow on SO_2 measured by DWP-OCT, a digital syringe pump (AL-1000,World Precision Instruments, Sarasota, FL) is used to introduce blood flow in the phantom vessel at a fixed SO_2 level (98.2%) corresponding to an arteriole. At the fixed SO_2 level, DWP-OCT SO_2 measurements are recorded at blood flow speeds from 0 to 17 mm/s. For each blood flow speed, SO_2 levels are also measured at the same position in the lumen of the phantom vessel.

3 Results

We observed *op* signal amplitude in the phantom vessel containing blood resulting from photothermal excitation with 770-nm and 800-nm light. In a control experiment, with the phantom vessel containing water, no *op* signal was detected in response to photothermal excitation. Three experiments were completed to investigate the functionality of the DWP-OCT system: en-face imaging of the blood vessel phantom, blood SO_2 measurement without flow, and influence of blood flow speed on SO_2 measurement.

3.1 *Phantom Image*

A two-vessel phantom was constructed to demonstrate DWP-OCT imaging of an arterial-venous vessel pair. Two 50-μm inner-diameter phantom vessels were attached to a sheet of white-colored copy paper to provide a scattering background for imaging. The two phantom vessels were filled with porcine blood, and digital syringe pumps were used to introduce flow (2.8 mm/s) in opposite directions in each phantom vessel (Fig. 4). Average flow speed was calculated by dividing the syringe pump infusion flow rate (0, 20, 40, 60, 80, 100, and 120 μL/h) by the phantom vessel's lumen cross-sectional area (1.96×10^3 μm^2).

3.2 *Blood SO_2 Measurement in Phantom Vessel without Flow*

DWP-OCT phase data was recorded over a time period of 1-s at the bottom of the lumen in one of the phantom vessels (Fig. 3). The *op* signal amplitude was determined for each 0.5-s data acquisition period by computing the fast Fourier transform (FFT) of the phase (φ_{sc}) data. For each 1-s of acquired DWP-OCT data, 15 sub-segments were analyzed with a 1/28-s offset between successive 0.5-s data segments. For each 0.5-s data segment, the *op* signal amplitudes at 380 and 400 Hz were calculated, and the SO_2 level was estimated according to Eq. (2). In the experiment, DWP-OCT data segments longer than 1-s were not recorded due to phase drift. Estimates of *op* were obtained using a moving average approach, which is preferred for short signal durations to reduce high-frequency noise. Phase noise in the *op* signal amplitude increases variance in the computed SO_2 levels (see error propagation model in Sec. 4.1).The mean of SO_2 values derived from 15 sub-segments gives a better estimate, and a moving window will smooth the time variation

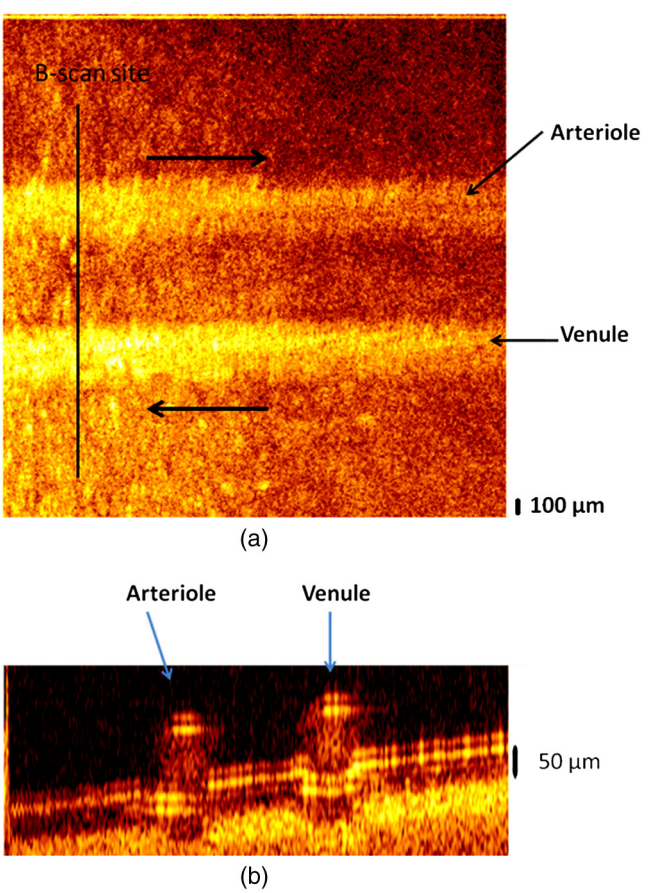

Fig. 4 (a) En-face image of an arterial-venous phantom vessel pair. (b) B-scan image at the indicated site. Arrows in (a) indicate blood flow direction.

of oxygen saturation. Averaging SO_2 values over the sub-segments suppresses the phase noise in the *op* signal amplitude.

To demonstrate DWP-OCT for blood SO_2 measurement, the six blood samples prepared at different SO_2 levels were measured (99.6%, 89.2%, 84.1%, 69.0%, 57.3%, and 3.0%) with a commercial blood oximeter (AVOXimeter 1000E, International Technidyne Corp., Edison, NJ). Each blood sample was separated into two volumes to ensure DWP-OCT and oximeter measurements could be carried out simultaneously, thus reducing measurement variation due to differences in reoxygenation. The DWP-OCT measurement time of a single blood sample was shorter than 30 min to minimize the effect of drift in the blood SO_2 levels (blood samples were deoxygenated by sodium dithionite).[46] The DWP-OCT SO_2 measurement results of the blood samples are shown in Fig. 5. Each plot indicates the SO_2 level deduced from Eq. (2) and derived from the 15 segments lasting 0.5-s each. The solid line (green) and dashed lines (red and blue) represent the mean and standard deviation, respectively, of the 15 segments' DWP-OCT SO_2 values. The SO_2 levels measured by a commercial oximeter are indicated in the right portion of each plot.

The six blood samples' SO_2 levels cover a substantially wider range than physiological variation [from 70% (veins) to 97 to 99% (arteries)]. For each measured level, the oximeter SO_2 measurement results are within the experimental error of DWP-OCT measurement values (Fig. 6). The AVOXimeter 1000E features a specified accuracy of $\pm 1\%$ and a precision of $\pm 0.5\%$ for blood SO_2 measurements.

3.3 *Influence of Blood Flow on DWP-OCT SO_2 Measurement*

To determine the impact of blood flow on DWP-OCT SO_2 measurement, we recorded the *op* signal amplitude in a 50-μm inner-diameter phantom blood vessel at different average blood flow speeds introduced by the syringe pump. For each DWP-OCT measurement, the SO_2 level was fixed at 98.2%. At increasing blood flow speeds, the *op* signal amplitude induced

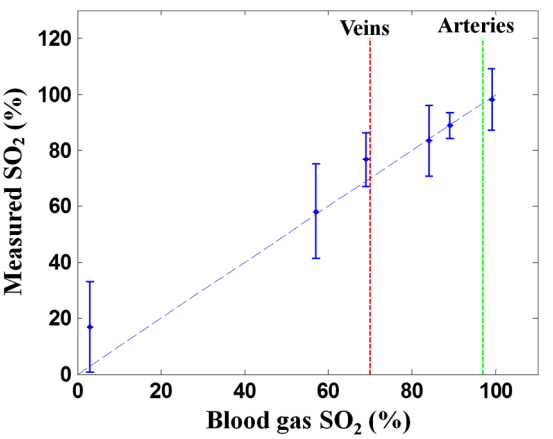

Fig. 6 Blood SO_2 level measured by DWP-OCT (vertical) versus oximeter values (horizontal). Blood is stationary for all measurements.

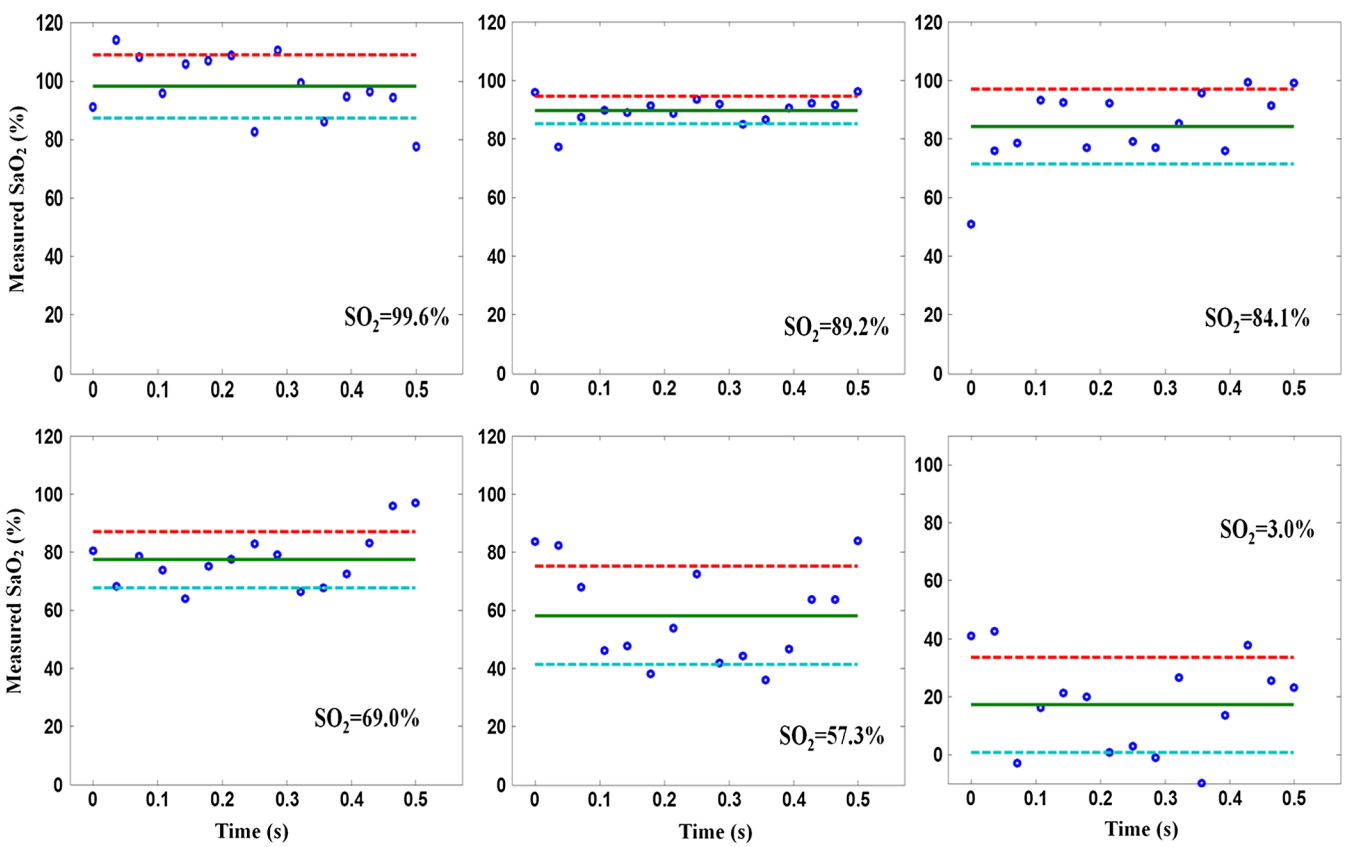

Fig. 5 Blood SO_2 levels measured in phantom vessels by DWP-OCT. The solid line represents the mean of 15 segments of 0.5 s each, and the dashed lines represent standard deviation. The SO_2 levels measured by a commercial oximeter are indicated in the right portion of each plot. Blood is stationary for all measurements.

by blood absorption of each photothermal excitation beam was reduced, as shown in Fig. 7(a). A substantial reduction (80%) in the op signal amplitude was observed at the greatest average blood flow speed (17 mm/s).

The DWP-OCT measurements were recorded at average blood flow speeds from stationary to 17 mm/s, and the op signal amplitudes for 770-nm (400-Hz) and 800-nm (380-Hz) light were normalized by respective amplitudes at the stationary condition, as shown in Fig. 7(b).

4 Discussion

In this study, we constructed a DWP-OCT system for the imaging and measurement of static and flowing blood SO_2 level in a phantom vessel. From Eq. (2), we find that the relative uncertainty in DWP-OCT blood SO_2 values can be written as

$$\frac{\delta SO_2}{SO_2} = \frac{(\alpha_{d2}\alpha_{o1} - \alpha_{d1}\alpha_{o2})(\delta\chi_{12}/\chi_{12})}{[\chi_{12}(\alpha_{o2} - \alpha_{d2}) - (\alpha_{o1} - \alpha_{d1})](\alpha_{d1}/\chi_{12} - \alpha_{d2})}. \tag{3}$$

The variation in χ_{12} [$\delta\chi_{12}/\chi_{12}$; see Eq. (4)] can originate from phase variation in the optical pathlength (op_1 or op_2) or the fluence (Φ_1 or Φ_2) of photothermal excitation beams.

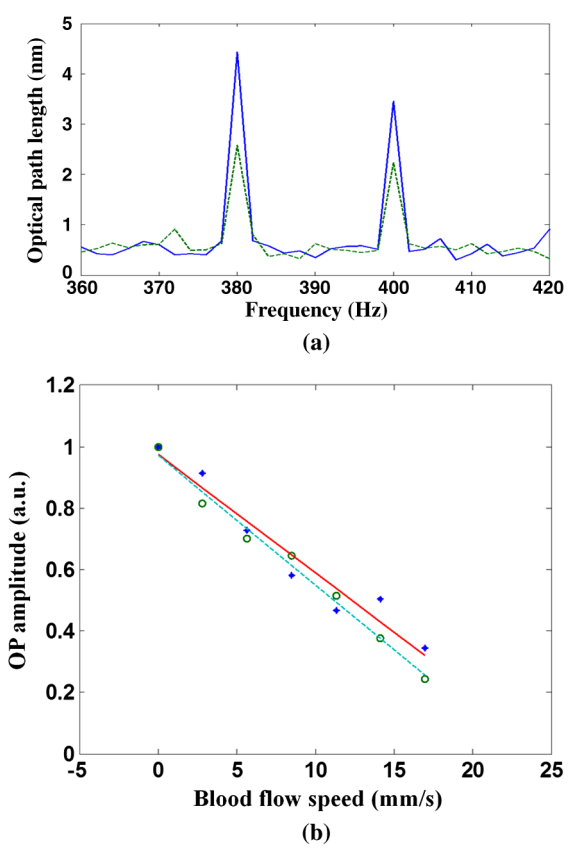

Fig. 7 (a) Reduction in the *op* signal amplitude at 800 nm (380 Hz) and 770 nm (400 Hz) from stationary (solid line) to increased average blood flow speed (dashed line, 8.5 mm/s) in a phantom blood vessel with a 50-μm inner diameter. (b) Normalized *op* signal amplitude versus average blood flow speed. Circle: *op* signal amplitude in response to 770-nm excitation, dashed line: linear fit, diamond: *op* signal amplitude in response to 800-nm excitation, solid line: linear fit.

$$\left(\frac{\delta\chi_{12}}{\chi_{12}}\right)^2 \approx \left(\frac{\delta op_1}{op_1}\right)^2 + \left(\frac{\delta op_2}{op_2}\right)^2 + \left(\frac{\delta\Phi_1}{\Phi_1}\right)^2 + \left(\frac{\delta\Phi_2}{\Phi_2}\right)^2. \tag{4}$$

We define the op signal-to-noise ratio [SNR; see Eq. (5)], where op is the optical pathlength signal amplitude in response to photothermal excitation (380 Hz or 400 Hz), and $\delta\, op$ corresponds to the optical pathlength variation due to either the DWP-OCT system or relative motion between the DWP-OCT source beams (PhS-OCT probe beam and photothermal excitation beams) and sample constituents.

$$\mathrm{SNR(d}B) = 10\log\left(\frac{op}{\delta op}\right). \tag{5}$$

4.1 *DWP-OCT Static Blood SO_2 Measurement Error*

In phantom vessel static blood SO_2 measurement, low-power (~2.8 mW) photothermal excitation light gives op amplitudes of 2 to 5 nm, and a 0.3-nm uncertainty in op amplitude gives a relative uncertainty $\delta op/op = 6$ to 15% (op SNR 8.2 to 12.2 dB). Laser power fluctuation can introduce a 2% uncertainty in $\delta\Phi/\Phi$. Based on Eqs. (3) and (4), the effect of the op SNR on the relative blood SO_2 measurement error ($\delta SO_2/SO_2$) was estimated (Fig. 8). Relative uncertainty in χ_{12} decreases with an increasing op SNR, as shown in Fig. 8(a). Relative uncertainty in DWP-OCT blood SO_2 increases with decreased SO_2 values, as shown in Fig. 8(b). At any blood SO_2 level, $\delta SO_2/SO_2$ increases with increasing relative uncertainty in χ_{12}. Each of the six measured blood samples' relative SO_2 measurement errors in a single (0.5-s) segment was deduced and plotted, as shown in Fig. 8(b), and they have values close to curves corresponding to 20% and 30% relative uncertainty in χ_{12}.

To reduce DWP-OCT's relative blood SO_2 measurement error to within 5% (SO_2 above 60%), relative uncertainty in χ_{12} must be less than 5%, requiring an op SNR above 15 dB ($\delta op/op$ below 3%). A substantial increase in DWP-OCT SO_2 measurement errors observed in 57.3% and 3% SO_2 blood levels are consistent with computed values, as shown in Fig. 8(b). To increase DWP-OCT blood SO_2 measurement accuracy and reliability, system phase stabilization is critical.

4.2 *Effect of Blood Flow on SNR of the Optical Pathlength Signal*

The accuracy of DWP-OCT SO_2 measurement at various blood flow speeds can be determined by analysis of the SNR of the op signal in response to laser excitation [Eq. (5)]. SNR degradation with respect to increasing blood flow speed, illustrated in Fig. 9(a), suggests that the most reliable DWP-OCT SO_2 measurements can be obtained at blood flow speeds up to 13 mm/s.

The SO_2 level is calculated for average blood flow speeds up to 17 mm/s, as shown in Fig. 9(b). The SO_2 measured by DWP-OCT is within the experimental error of values measured by a commercial oximeter for average blood flow speeds less than 13 mm/s. A 13-mm/s average blood flow speed is found in retinal arterioles[47] 30 to 40 μm in diameter. Relative blood SO_2 measurement error increases with increasing blood flow speed, as shown in Fig. 9(c). The op SNR is a critical factor that determines accuracy of measured SO_2 levels, as shown in Fig. 9(b). The results suggest that when the op SNR degradation exceeds 10 dB, SO_2 levels measured by DWP-OCT are

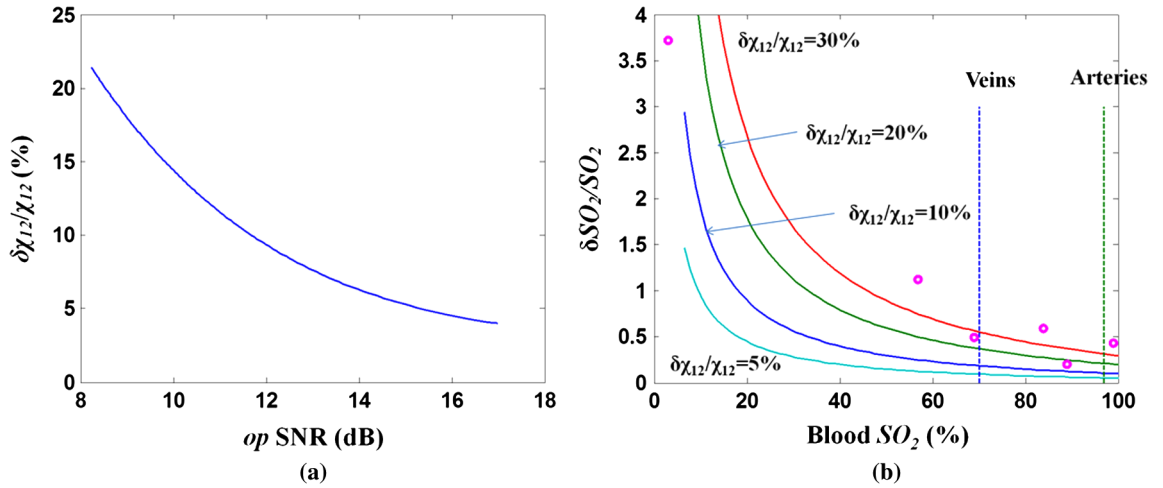

Fig. 8 (a) Relative χ_{12} error ($\delta\chi_{12}/\chi_{12}$) versus *op* SNR.(b) Relative blood SO_2 measurement error ($\delta SO_2/SO_2$) versus SO_2 for various levels of relative χ_{12} error. Horizontal axis: blood SO_2 level, vertical axis: relative error of SO_2. Solid curves represent conditions when the relative variations of χ_{12} are 5%, 10%, 20%, and 30%. Dashed lines: SO_2 of veins (70%) and arteries (97%), circles: relative blood SO_2 measurement error in six blood samples.

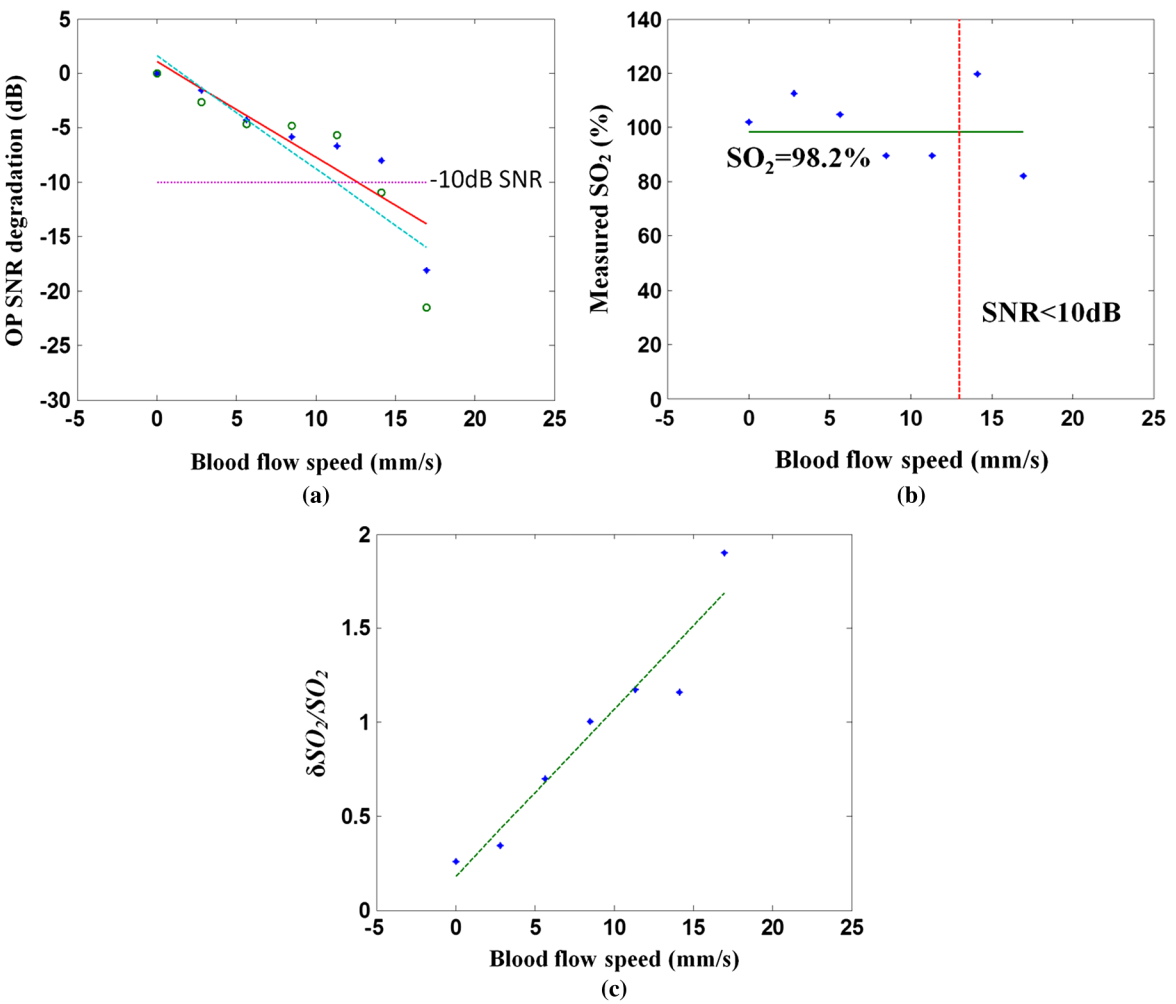

Fig. 9 (a) SNR degradation versus blood flow speed. Circle: SNR in response to 770-nm excitation, dashed line: linear fit, diamond: SNR in response to 800-nm excitation, solid line: linear fit, dotted line: 10-dB SNR *op* degradation. (b) SO_2 measurement in blood vessel phantom at various blood flow speeds. Diamond: SO_2 measured by DWP-OCT, solid line: SO_2 measured by oximeter (98.2%), dashed line: threshold speed above which SNR degradation exceeds 10 dB. (c) Relative blood SO_2 measurement error ($\delta SO_2/SO_2$) for a single segment (0.5 s) versus blood flow speed. Dashed line is linear fit.

no longer reliable. Experimental results suggest that a DWP-OCT system utilizing low-power (~2.8 mW) photothermal excitation has sufficient stability and sensitivity to measure SO_2 levels in a 50-μm-diameter stationary blood vessel phantom with average blood flow speeds from stationary up to 13 mm/s.

Brownian motion and blood flow can also contribute to an increased op signal noise floor; in the blood flow experiments reported here, the difference in refractive indices between red blood cells (RBC) and blood plasma is one source of increased op signal noise. The time dependent optical pathlength $[op(t)]$ of the probe beam traveling through the phantom vessel lumen can be expressed as

$$op(t) = n_{RBC} l_{RBC}(t) + n_{\text{plasma}} l_{\text{plasma}}(t), \tag{6}$$

where n_{RBC} and n_{plasma} are the group refractive indices of red blood cells and plasma, respectively; and l_{RBC} and l_{plasma} are the physical pathlengths that probe beam travels through RBC and blood plasma, respectively. The values of l_{RBC} and l_{plasma} vary randomly due to blood flow; a higher blood flow speed will cause op signal amplitude to change more rapidly, as indicated in Eq. (6), which results in an increased op signal noise floor between successive A-scans. In the case of stationary blood, Brownian RBC motion contributes to the op signal noise. For the phantom blood vessel tested here (with a 50 μm inner-diameter), the effect of Brownian RBC motion on op signal noise is approximately equivalent to the increase associated with a 6-mm/s blood flow speed relative to the stationary state.[48] An increased op signal noise floor is observed in a larger vessel (300 μm innerdiameter) due to a longer physical pathlength. The SO_2 measurement has also been recorded in a 300-μm-diameter phantom blood vessel. At an equivalent average blood flow speed (11.8 mm/s), the op signal noise floor (1.82 nm) in the larger phantom vessel (300 um innerdiameter) increases by 1.3 nm over the signal noise floor (0.52 nm) in the phantom vessel with a 50-μm innerdiameter.

For *in vivo* measurements, the relative motion between the DWP-OCT source beams and the bulk tissue is an additional noise source that degrades the op SNR. Tissue motion artifacts can be suppressed by increasing either the modulation frequency or the DWP-OCT A-scan rate. SS laser sweep rates of up to 5 MHz have been demonstrated.[49] A higher modulation frequency will require photothermal excitation lasers with greater instantaneous power (corresponding to a shorter excitation period) to maintain fluence at the same level as the system presented here. In studies reported here, the incident radiant power (~2.8 mW) is within the ANSI limits for skin. For retinal applications, the photothermal excitation power must be less than 0.75 mW.

Acknowledgments

This study was partially supported by NIH KL2 training grants (Parent Grant Nos. UL1RR025767 and KL2RR025766); by the San Antonio Area Foundation (Grant No. 130977); and by research support from Carl Zeiss Meditec to RVK and TEM, from the Department of Veterans Affairs (VA MERIT Award) to TQD, and by the NIH (R01 EY018855 and R01 EY014211) to TQD. The authors also gratefully acknowledge support from the National Institutes of Health (NIH R01EY016462).

References

1. P. Carmeliet and R. K. Jain, "Angiogenesis in cancer and other diseases," *Nature* **407**(6801), 249–257 (2000).
2. P. Carmeliet, "Angiogenesis in life, disease and medicine," *Nature* **438**(7070), 932–936 (2005).
3. R. A. Linsenmeier and C. M. Yancey, "Effects of hyperoxia on the oxygen distribution in the intact cat retina," *Investig. Ophthalmol. Vis. Sci.* **30**(4), 612–618 (1989).
4. L. Padnick-Silver et al., "Retinal oxygenation and oxygen metabolism in Abyssinian cats with a hereditary retinal degeneration," *Investig. Ophthalmol. Vis. Sci.* **47**(8), 3683–3689 (2006).
5. D. Y. Yu, S. J. Cringle, and E. N. Su, "Intraretinal oxygen distribution in the monkey retina and the response to systemic hyperoxia," *Investig. Ophthalmol. Vis. Sci.* **46**(12), 4728–4733 (2005).
6. R. N. Glud et al., "Planar optrodes: a new tool for fine scale measurements of two-dimensional O^2 distribution in benthic communities," *Mar. Ecol. Prog. Ser.* **140**, 217–226 (1996).
7. C. Y. Yu et al., "Oxygen distribution and consumption in rat lower incisor pulp," *Arch. Oral Biol.* **47**(7), 529–536 (2002).
8. H. Y. Cheng et al., "Structural and functional MRI reveals multiple retinal layers," *Proc. Natl. Acad. Sci. U.S.A.* **103**(46), 17525–17530 (2006).
9. B. A. Berkowitz et al., "Subnormal retinal oxygenation response precedes diabetic-like retinopathy," *Investig. Ophthalmol. Vis. Sci.* **40**(9), 2100–2105 (1999).
10. T. Q. Duong et al., "Layer-specific anatomical, physiological and functional MRI of the retina," *NMR Biomed.* **21**(9), 978–996 (2008).
11. A. Karni et al., "Functional MRI evidence for adult motor cortex plasticity during motor skill learning," *Nature* **377**(6545), 155–158 (1995).
12. P. J. Koopmans, M. Barth, and D. G. Norris, "Layer-specific BOLD activation in human V1," *Hum. Brain Mapp.* **31**(9), 1297–1304 (2010).
13. K. R. Denninghoff et al., "Retinal venous oxygen saturation and cardiac output during controlled hemorrhage and resuscitation," *J. Appl. Physiol.* **94**(3), 891–896 (2003).
14. M. Hammer and D. Schweitzer, "Quantitative reflection spectroscopy at the human ocular fundus," *Phys. Med. Biol.* **47**(2), 179–191 (2002).
15. P. L. Madsen and N. H. Secher, "Near-infrared oximetry of the brain," *Prog. Neurobiol.* **58**(6), 541–560 (1999).
16. M. G. Sowa et al., "Noninvasive assessment of regional and temporal variations in tissue oxygenation by near-infrared spectroscopy and imaging," *Appl. Spectrosc.* **51**(2), 143–151 (1997).
17. A. K. Dunn et al., "Simultaneous imaging of total cerebral hemoglobin concentration, oxygenation and blood flow during functional activation," *Opt. Lett.* **28**(1), 28–30 (2003).
18. D. Izhaky et al., "Functional imaging using the retinal function imager: direct imaging of blood velocity, achieving fluorescein angiography-like images without any contrast agent, qualitative oximetry, and functional metabolic signals," *Jpn. J. Ophthalmol.* **53**(4), 345–351 (2009).
19. R. D. Shonat and A. C. Kight, "Oxygen tension imaging in the mouse retina," *Ann. Biomed. Eng.* **31**(9), 1084–1096 (2003).
20. R. Zuckerman, J. E. Cheasty, and Y. P. Wang, "Optical mapping of inner retinal tissue PO_2," *Curr. Eye Res.* **12**(9), 809–825 (1993).
21. A. S. Golub, M. A. Tevald, and R. N. Pittman, "Phosphorescence quenching microrespirometry of skeletal muscle in situ," *Am. J. Physiol. Heart Circ. Physiol.* **300**(1), H135–H143 (2011).
22. A. G. Tsai et al., "Microvascular and tissue oxygen gradients in the rat mesentery," *Proc. Natl. Acad. Sci. U.S.A.* **95**(12), 6590–6595 (1998).
23. L. W. Lo, C. J. Koch, and D. F. Wilson, "Calibration of oxygen-dependent quenching of the phosphorescence of Pd-meso-tetra (4-carboxyphenyl) porphine: a phosphor with general application for measuring oxygen concentration in biological systems," *Anal. Biochem.* **236**(1), 153–160 (1996).
24. G. Helmlinger et al., "Interstitial pH and pO_2 gradients in solid tumors in vivo: high-resolution measurements reveal a lack of correlation," *Nat. Med.* **3**(2), 177–182 (1997).
25. D. Huang et al., "Optical coherence tomography," *Science* **254**(5035), 1178–1181 (1991).
26. A. F. Fercher et al., "Measurement of intraocular distances by backscattering spectral interferometry," *Opt. Commun.* **117**(1–2), 43–48 (1995).

27. G. Häusler and M. W. Lindner, "'Coherence radar' and 'spectral radar'-new tools for dermatological diagnosis," *J. Biomed. Opt.* **3**(1), 21–31 (1998).
28. R. Huber et al., "Amplified, frequency swept lasers for frequency domain reflectometry and OCT imaging: design and scaling principles," *Opt. Express* **13**(9), 3513–3528 (2005).
29. F. Robles, R. N. Graf, and A. Wax, "Dual window method for processing spectroscopic optical coherence tomography signals with simultaneously high spectral and temporal resolution," *Opt. Express* **17**(8), 6799–6812 (2009).
30. R. Leitgeb et al., "Spectral measurement of absorption by spectroscopic frequency-domain optical coherence tomography," *Opt. Lett.* **25**(11), 820–822 (2000).
31. D. J. Faber and T. G. van Leeuwen, "Are quantitative attenuation measurements of blood by optical coherence tomography feasible?," *Opt. Lett.* **34**(9), 1435–1437 (2009).
32. J. Yi and X. Li, "Estimation of oxygen saturation from erythrocytes by high-resolution spectroscopic optical coherence tomography," *Opt. Lett.* **35**(12), 2094–2096 (2010).
33. F. E. Robles et al., "Molecular imaging true-colour spectroscopic optical coherence tomography," *Nat. Photon.* **5**(12), 744–747 (2011).
34. D.C. Adler et al., "Photothermal detection of gold nanoparticles using phase-sensitive optical coherence tomography," *Opt. Express* **16**(7), 4376–4393 (2008).
35. M. C. Skala et al., "Photothermal optical coherence tomography of epidermal growth factor receptor in live cells using immunotargeted gold nanospheres," *Nano Lett.* **8**(10), 3461–3467 (2008).
36. A. S. Paranjape et al., "Depth resolved photothermal OCT detection of macrophages in tissue using nanorose," *Biomed. Opt. Express* **1**(1), 2–16 (2010).
37. R. V. Kuranov et al., "Depth-resolved blood oxygen saturation measurement by dual-wavelength photothermal (DWP) optical coherence tomography," *Biomed. Opt. Express* **2**(3), 491–504 (2011).
38. R. V. Kuranov et al., "In vivo depth-resolved oxygen saturation by dual-wavelength photothermal (DWP) OCT," *Opt. Express* **19**(24), 23831–23844 (2011).
39. R. V. Kuranov et al., "Gas-cell referenced swept source phase sensitive optical coherence tomography," *IEEE Photon. Technol. Lett.* **22**(20), 1524–1526 (2010).
40. K. Santhanam, "Clock system design for quadrupling the frequency of reference clock for a swept source spectral domain optical coherence tomography," Master Thesis, The University of Texas at Austin (2009).
41. A. M. Rollins and J. A. Izatt, "Optimal interferometer designs for optical coherence tomography," *Opt. Lett.* **24**(21), 1484–1486 (1999).
42. B. J. Vakoc et al., "Phase-resolved optical frequency domain imaging," *Opt. Express* **13**(14), 5483–5493 (2005).
43. M. Wojtkowski et al., "Ultrahigh-resolution, high-speed, Fourier domain optical coherence tomography and methods for dispersion compensation," *Opt. Express* **12**(11), 2404–2422 (2004).
44. T. Wu et al., "Spectral phase based k-domain interpolation for uniform sampling in swept-source optical coherence tomography," *Opt. Express* **19**(19), 18430–18439 (2011).
45. A. J. Welch and M. J. C. van Gemert, *Optical-Thermal Response of Laser-Irradiated Tissue, Laser, Photonics, and Electro-Optics*, Plenum Press, New York, NY (1995).
46. K. Briely-Sabo and A. Bjornerud, "Accurate de-oxygenation of ex vivo whole blood using sodium Dithionite," *Proc. Intl. Sot. Mag. Reson. Med.* **8**, 2025 (2000).
47. Y. P. Ma et al., "On-line measurement of the dynamic velocity of erythrocytes in the cerebral microvessels in the rat," *Microvas. Res.* **8**(1), 1–13 (1974).
48. T. Binzoni et al., "Non-invasive laser Doppler perfusion measurements of large tissue volumes and human skeletal muscle blood RMS velocity," *Phys. Med. Biol.* **48**(15), 2527–2549 (2003).
49. W. Wieser et al., "Multi-Megahertz OCT: high quality 3D imaging at 20 million A-scans and 4.5 GVoxels per second," *Opt. Express* **18**(14), 14685–14704 (2010).